Chapter 5

Resistive Detection and Damping

The oscillation frequencies of charged particles confined in the harmonic well can be non-destructively interrogated and measured. Particle motions produce alternating currents in the conducting trap electrodes. These are monitored by sending them through a large effective resistor and observing the resulting alternating voltage drop at the frequency of the particle oscillation. A schematic version of this detection is shown in Fig. 5.1. The electron axial motion, and the antiproton's axial and cyclotron motion are detected similarly, at easily accessible radiofrequencies.

This scheme is also effective in damping the particles motion. Power dissipated in the resistor is lost from the particle motion, cooling this motion into thermal equilibrium with the resistor. The effective resistor is kept near 4.2 K to minimize noise and particle amplitudes.

The resistive damping rate and resulting detection linewidth of a single particle of mass m and charge q can be estimated by a simple model. The induced current I dropped across a resistor R produces a potential drop, which in turn produces an electric field at the center of the trap, resulting in an axial force on the particle of

$$\mathbf{f} = q\mathbf{E} = -q\kappa\left(\frac{IR}{2z_0}\right)\hat{\mathbf{z}}, \tag{5.1}$$

where κ is a geometrical coefficient, and $2z_0$ the axial dimension of the trap shown in Fig. 3.1. (If the detection electrodes were infinite plates of separation $2z_0$, κ would equal unity.) For the axial detection shown in Fig. 5.1, κ is equivalent

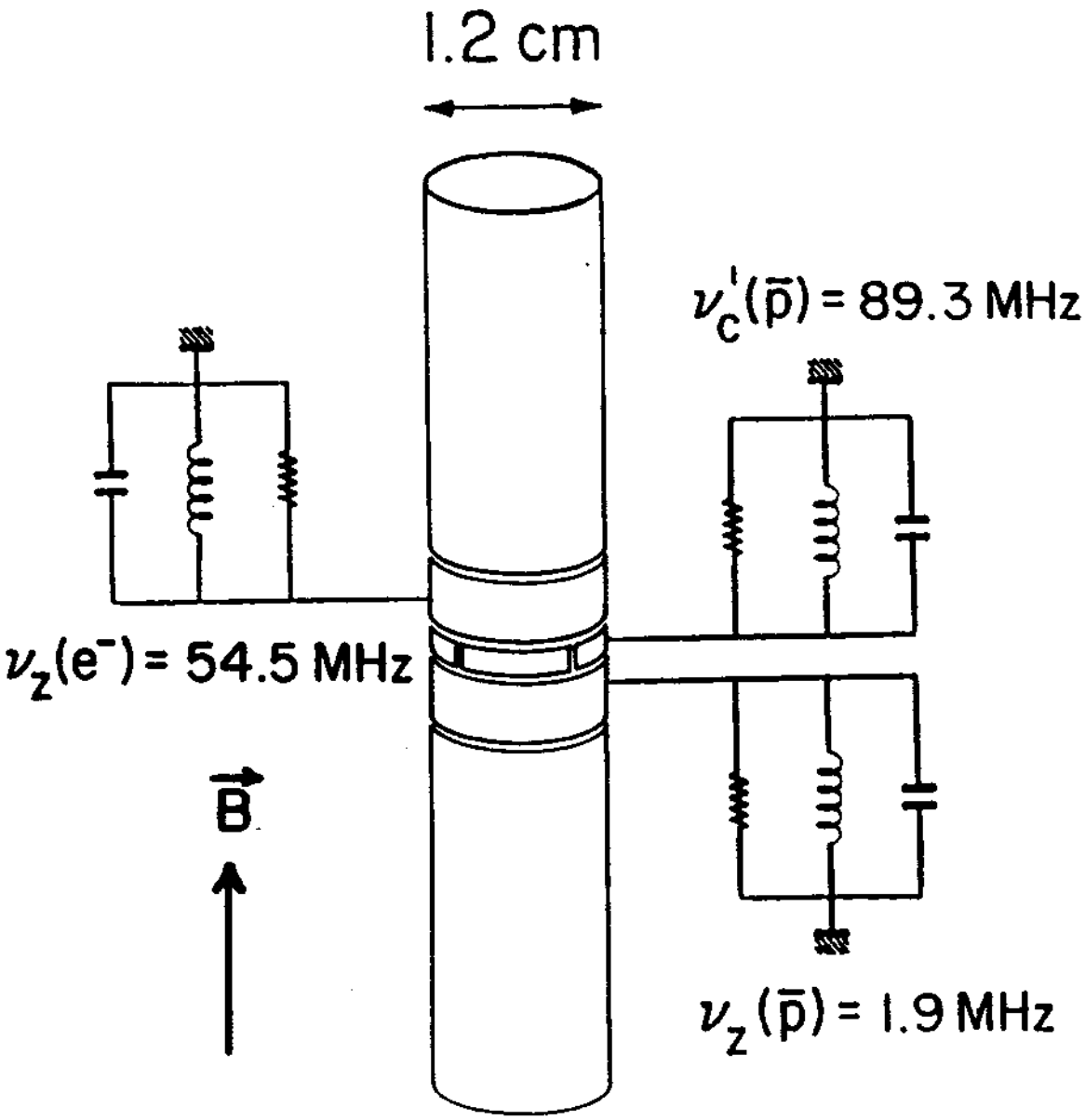

Figure 5.1: Schematic circuit for resistive detection and damping of the axial and cyclotron motions of antiprotons (protons) and electrons.

to the coefficient d_1 for the asymmetric voltage boundary condition applied to the compensation electrodes. (An analogous situation exists for detection and damping of the cyclotron motion with a resistor across two opposing quadrants of the segmented ring, except that z_0 is replaced with ρ_0 and κ is denoted κ' reflecting a different geometry).

The size of the damping force (f $\rightarrow$ 0 as $v \rightarrow 0$) is proportional to the size of the induced current, which depends upon the particle velocity (i.e. the square root of the axial energy). The particle axial energy E_z is dissipated in the resistor at a rate

$$\frac{dE_z}{dt} = -\dot{z}f = I^2 R_z. \tag{5.2}$$

The induced current is then

$$I = d_1 \left(\frac{q}{2z_0}\right) \dot{z}. \tag{5.3}$$

Noting that the damping force can be written as $-m\gamma_z \dot{z}$, the axial damping coefficient γ (or linewidth $= \gamma/2\pi$) for a single particle, using (5.1) and (5.2), is

$$(\gamma_z)_1 = \left(\frac{qd_1}{2z_0}\right)^2 \frac{R_z}{m}, \tag{5.4}$$

and analogously the single particle cyclotron damping coefficient is

$$(\gamma_c)_1 = \left(\frac{q\kappa'}{2\rho_0}\right)^2 \frac{R_c}{m}. \tag{5.5}$$

The damping time constant $\tau = 2\pi/\gamma$ (or linewidth $= 1/\tau$) depends upon the charge state and mass as q^2/m. Thus a proton (or antiproton) takes 1836 times longer to damp than an electron in the same trap for the same R and the linewidth will be 1836 times narrower.

The damping also depends on the size of the trap (z_0 or ρ_0), and on the geometry and location of the chosen detection electrode (d_1 or κ'). A small trap maximizes the damping and produces the largest detection signals. Since the compensation electrodes are large and closer to the trap center than are the endcaps, by detecting on them we improve our detection sensitivity by a factor of $d_1^2/c_1^2 = 7.2$.

To first order, the center of mass motion of a cloud of N particles oscillate at the same frequency as a single particle [115]. The generalized version for the total induced current is

$$I = d_1 \left(\frac{Nq}{2z_0}\right) \dot{Z}, \tag{5.6}$$

where $Z \equiv \sum_k^N z_k/N$ is the center of mass coordinate for the N particles.

For pure center of mass motion (uncoupled from other motions), the damping coefficient for N particles is increased to

$$\gamma_N = N\gamma_1. \tag{5.7}$$

Thus, the center of mass motion of N particles damps with a time constant proportional to 1/N of the single particle damping time. Energy present in the internal degrees of freedom is not as easily removed since it must first couple to the center of mass motion before it can damp.

5.1 Detection Amplifier

Resonant Circuits

In addition to the trap size, detection geometry, and particle number, the damping coefficient is linearly dependent on the size of the resistor R_z or R_c. In practice, this resistance is realized by placing an inductor L in parallel with the trap electrode and feedthrough capacitance (Fig. 5.1). On resonance, L cancels C so that the impedance of the circuit is purely resistive. The small induced current is observed as an rms voltage V_s across the resonant circuit. We select L such that each tuned circuit resonates at the appropriate resonant frequency of the motion to be detected.

The physical LC circuit has finite resistive losses and an observable resonant bandwidth. The resonant circuit quality factor $Q=\nu/\Delta\nu$, is a measure of the effective parallel resonance resistance R. The width $\Delta\nu$ partially results from loss of RF energy in the resonator coil and walls of the cavity due to the skin effect. Skin depths in copper at 300 K for RF frequencies in the 1→ 100 MHz range are about $\delta = 0.07 \rightarrow 0.007$ mm respectively, scaling with the conductivity for lower

temperatures. Circuit Q's also depend on several aspects of construction such as coil wire spacing, dimensions and joint quality [79,110]. In addition, the detection trap electrode is capacitively coupled to adjacent electrodes ($C \approx 1-3pF$), so that lossy couplings to adjacent electrodes must be avoided. For a resonant parallel LCR circuit, $R = Q\omega L = 1/\Delta\omega C$. To maximize the effective parallel resonance resistance, we desire Q and L as high as possible and C as small as possible.

The typical inductance required for each detection circuit is shown in Table 5.1. Each inductor is mounted in a 5 cm long, 3.5 cm ID cylindrical copper cavity. The cavity is bolted firmly for good grounding and heat sinking to the gold plated electronics region just below the liquid helium dewar and above the trap vacuum enclosure (Chapter 3). The three cavities are made large to maximize the volume (proportional to the energy stored) to the surface area (proportional to the cavity surface losses). Larger cavities were not possible because space near the vacuum enclosure is limited and the region below the trap enclosure is not available because of the need to interface to the antiproton beamline at LEAR.

The inductor for the 1.9 MHz axial antiproton circuit is made of 0.1 mm diameter enameled copper wire and is a 4.5 cm long, single layer coil ($\approx$ 200 turns) with a diameter of 2.4 cm. The antiproton cyclotron and electron axial resonant circuits have inductors wound from 2 mm diameter silver plated OFHC copper wire ($\approx$ 3-5 turns). In all cases, the lower end is attached to a trap feedthrough and the appropriate trap electrode through a hole in the cavity bottom, and the upper end is RF grounded to the cavity wall using low loss capacitors. The rms voltage is picked off the coil with a tap typically located between 1/3 and 2/3 up from the RF ground. The tap is capacitively coupled to the gate input of a GaAs field effect transistor (FET).

GaAs FET Pre-Amplifier

Pre-amplifiers, shown schematically in Fig. 5.2, are mounted close to the trap and cooled to 4 K. A GaAs FET and an impedance matching π network are used to match the small signal V_s to a 50 Ω transmission line and drive it. The transistor is a Mitsubishi GaAs FET MGF1100 (dual-gate N-channel Schottky barrier gate

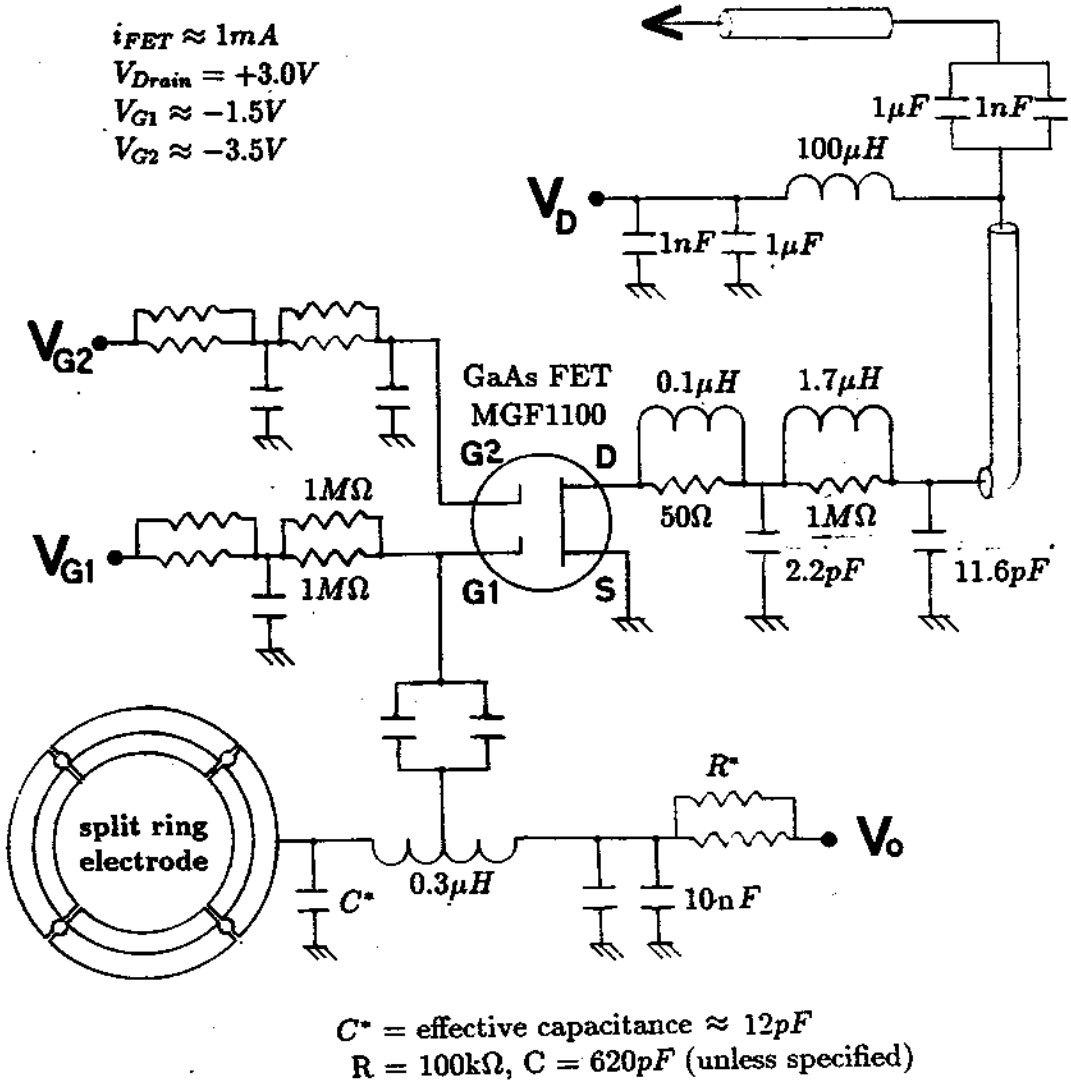

Figure 5.2: Detection resonant circuit, Field Effect Transistor circuit, and π network used for the 89 MHz cryogenic amplifier.

type). It is specified for operation in the 500 MHz to 4 GHz region and has a noise figure of 2.5 dB at 4 GHz. GaAs transistors perform well at 4 K, though the currently used FET is in a region far below their normal specifications. An FET is appropriate for for this application in that high input impedances are possible, though heat dissipated in the FET increases the helium boiloff and keeps the channel temperature above 4 K.

In Fig. 5.2 circuit values shown for direct detection of the antiproton cyclotron oscillation near 89 MHz. The rms voltage signal V_s is capacitively coupled to gate 1 (G1). Gate 2 (G2) provides capacitive isolation between the drain (output) and G1 (input). The Source (S) is held at ground and the signal output on the Drain (D) goes to a π network to impedance match the FET output to a 50 Ω transmission line. The values here match an output impedance of about 20 kΩ at 89 MHz to 50 Ω. (The axial amplifiers are similar except for modifications of the capacitor and inductor values to accomodate different frequencies.)

The amplifier has near unity voltage gain, but a power gain of 400 capable of driving 50 Ω. The drain is biased at +3 Volts with respect to the grounded source. Gates 1 and 2 both have dc biases supplied through RF filters. The bias ranges between $\pm$ 5 Volts, where -5 Volts stops the current flow between the source and the drain. The dc bias on the gates are adjusted (typically Gate 2 is almost completely open and Gate 1 is almost closed) so that the drain-source current is $\approx$ 1 mA. At such operating conditions the power dissipated into the cryogenic system is about 3 mW per amplifier, a significant but manageable heat load if all three are operated continuously since typical power dissipation in the cryogenic system is still only 27 mW.

The FET and π network circuit are contained in an RF enclosed region on the top of the copper cavities used to house the inductors. The resonant circuit region and the amplifier region are separated by a grounded copper partition that has a small hole for the tap lead to be connected to gate 1. In the amplifier region, the four leads from the FET straddle two sides of a piece of grounded double-sided copper clad G-10 circuit board. The gate dc leads, filters, and RF input are on one side, and the source, drain, and π network are on the other to minimize

possibilities of feedback.

Metal film resistors are used throughout because of their good stability over wide temperature ranges. Since the failure rate can be as high a 5%, we often place two in parallel as shown in Fig. 5.2 to insure that if one fails we can continue operating.

Measured Q's

The output signal of the cold FET-π network system is transmitted up and out of the magnet bore on a 1 meter long S.S. coaxial cable, ac coupled from the drain (which has a dc bias on it) and is further amplified. In Fig. 5.3 we show the noise spectra for each of the three amplifiers, when they near 4 K and are connected to the appropriate trap electrodes (the trap contains no particles). The three spectra shown are each observed with a 1 kHz bandwidth using a HP 8562A spectrum analyzer. The same broadband amplification was used for each trace ($\approx$+60 dB using six Anzac AM-107 in series). The noise resonance [108] is predominantly the thermal Johnson noise of the 4 K resonant circuit (the resistor) given by

$$v_R(rms) = \sqrt{4k_B RTB} \tag{5.8}$$

where B is the detection bandwidth in Hz, k_B is the Boltzman constant, and R the effective resistance at temperature T.

The Q of each resonant circuit is determined from the width of the noise resonance. The $Q=\nu/\Delta\nu$ with the resonance width $\Delta\nu$ defined as -3 dB down from the maximum power. In terms of these rms spectra, $\Delta\nu$ is measured at 0.707 V_{peak}.

In Table 5.2, the measured Q's and effective resistances for each circuit are shown, along with the inferred linewidths and damping time constants using Eqs. 5.4, 5.5, and 5.7. We note that the Q of the cyclotron amplifier is lower than the electron axial amplifier, which is at a lower frequency. This is likely due to RF grounding problems associated with the ring and the compromises made to accomodate all the detection and drive constraints on the neighboring electrodes.

Table 5.1: Actual tuned circuit parameters for the three resonant circuits tuned to ν_z (antiproton), ν_z (electron), and ν_c' (antiproton).

Circuit	ω	C	L	Q(300K)	Q(4K)	$\Delta\nu(300K \rightarrow 4K)$
$\nu_z(\overline{p})$	2π(1.91 MHz)	≈18pF	390μH	55	150	+55kHz (2.9%)
$\nu_z(e^-)$	2π(54.5 MHz)	≈18pF	0.5μH	180	1020	+1.23 MHz (2.3%)
$\nu_c'(\overline{p})$	2π(89.3 MHz)	≈12pF	0.3μH	210	520	+1.86 MHz (2.0%)

Circuit	R=QωL	$\gamma_N/2\pi$	$\tau_N = \tau_1/N$ †
$\nu_z(\overline{p})$	$7.0 \times 10^5\Omega$	N(8.4 mHz)	18/N sec
$\nu_z(e^-)$	$1.7 \times 10^5\Omega$	N(3.7 Hz)	0.3/N sec
$\nu_c'(\overline{p})$	$7.8 \times 10^4\Omega$	N(0.8 mHz)	190/N sec

† Estimated damping time of center of mass motion

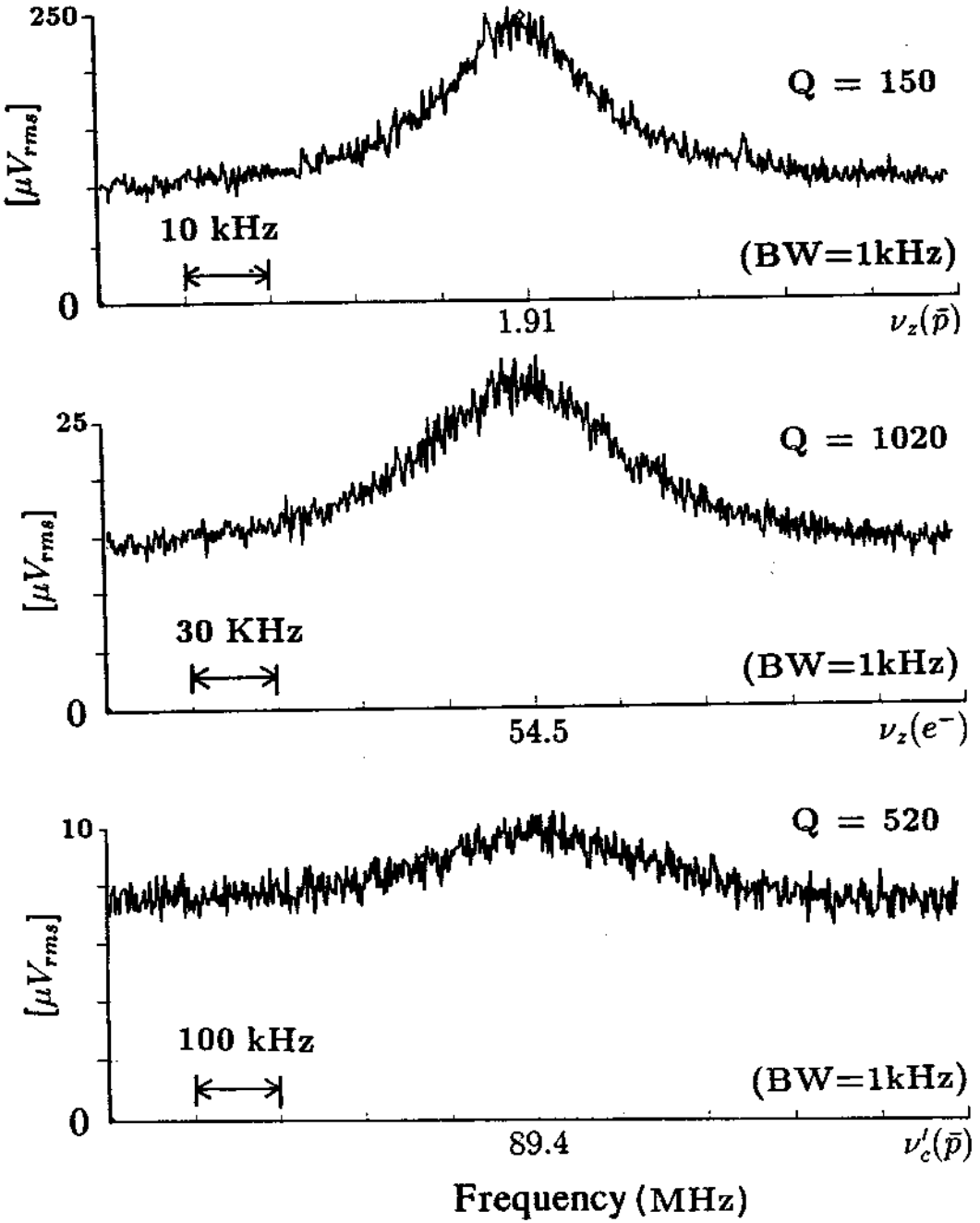

Figure 5.3: Voltage induced across the LCR resonant circuit at 4 K for the three amplifiers using the same broadband amplification for (a) the detection of $\nu_z(\bar{p})$, (b) the detection of $\nu_z(e^-)$, and (c) the detection of $\nu_c'(\bar{p})$.

5.2 Drive and Detection Scheme and Wiring

Gain and Detection

The two general detection techniques shown schematically in Fig. 5.4 are; (1) the direct observation of the induced voltage amplitude V_s as a function of frequency by Fourier transformation or by observing the rectified power in a given bandwidth (denoted 'square law detection' since $V_{out} \propto V_{in}^2$) and (2) the observation of the particle oscillation or center of mass motion of many particles using phase sensitive detection techniques. For both schemes, it is often desirable to apply external RF drives to the particles. Using drives one can resonantly increase the particle amplitude resulting in increased signal to noise, and/or drive the particles at a known phase.

Direct amplitude signals are observed either on a spectrum analyzer, or by square law detection as a function of frequency. The general scheme for amplitude and/or phase sensitive detection is shown in Fig. 5.4. The largest problems to overcome with phase sensitive detection are those related to insufficient damping, particle impurities (by causing dephasing by collisions), and direct feedthrough of the phase defining excitation drive. Elimination of direct feedthrough for coherent axial detection is accomplished by modulating the ring potential which generates FM sidebands on the particle axial motion. By driving on the sidebands, the drive is isolated from the preamplifier which is tuned to the fundamental axial motion [13]. With a coherent signal, the axial particle motion can be held fixed with a phase sensitive frequency lock using feedback voltage to the endcaps (or to the ring).

Phase sensitive detection techniques can be performed with the direct antiproton cyclotron signal as well but the direct feedthrough is more difficult to eliminate since, in practice, it is more difficult to modulate the magnetic field in an analogous way to the voltage modulation. A properly balanced drive helps in reducing the direct feedthrough. Another scheme is to alternate drive and detection cycles as is done in the pulsed NMR measurements.

Radio frequency drives applied at an appropriate frequency and symmetry

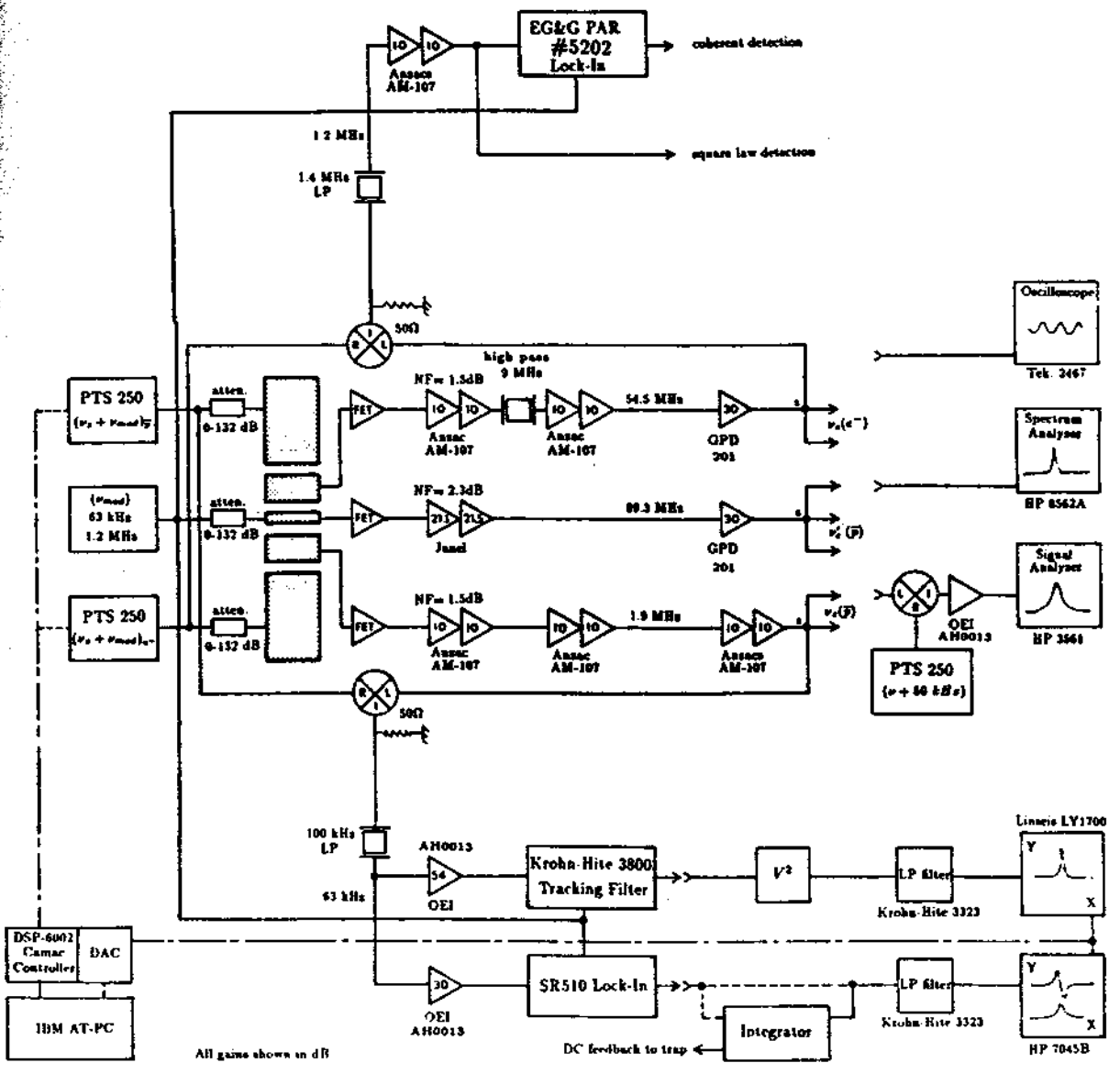

Figure 5.4: Gain and general detection scheme used for square law and phase sensitive detection of the antiproton axial and cyclotron motions ($\nu_z(\overline{p})$ and $\nu_c'(\overline{p})$) and the electron axial motion ($\nu_z(e^-)$).

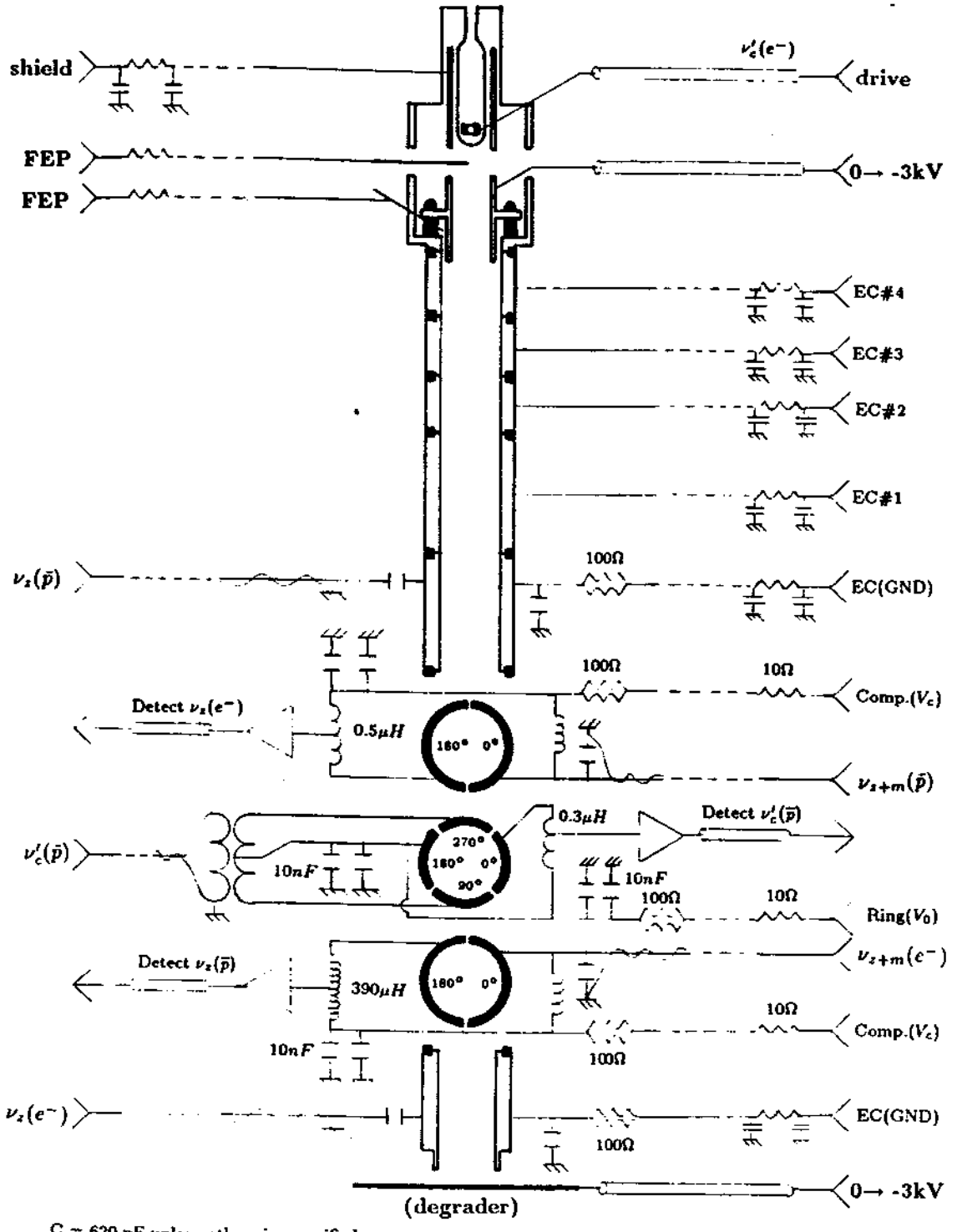

Figure 5.5: The trap wired showing all drives, dc lines, and RF filters. The filter values are compromised so that fast ramping of trap potentials can be done in addition to the resonant measurments.

on the trap are used to couple orthogonal particle motions. An example is the technique of motional sideband cooling to reduce the magnetron orbit radius by coupling to the axial motion (which is resistively damped). This form of sideband cooling requires application of a drive at $\nu_z + \nu_m$, with a symmetry that gives x and z gradients to the applied electric field [114,96]. Analogous applications are used to couple other orthogonal motions such as ν_c' with ν_z [22] and ν_c' with ν_m [85].

Trap Wiring and Filtering

In Fig. 5.5, we show the complete RF and dc wiring of the trap. We note that the filters on the dc leads have a rather small RC time constant. For high precison mass spectroscopy, it would be desirable to have these lines much more tightly filtered, but for these initial studies we also needed to retain the ability to quickly ramp the potential on the harmonic well for destructive energy measurements [45].

To simultaneously detect and damp the three motions $\nu_z(e^-)$, $\nu_z(\overline{p})$, and $\nu_c'(\overline{p})$ we connect the three amplifiers to electrodes making up the harmonic well as shown in Fig. 5.5. The direct cyclotron detection is on one quadrant of the ring, and the two axial amplifiers are on half segments of the split compensation electrodes. The opposing segments are left to accomodate magnetron sideband drives for both the electron and antiprotons, which both need the symmetry mentioned earlier.

The problem of capacitive coupling between the detection systems on the ring and compensation electrodes is solved with the detection side alternated on opposite sides as shown in Fig. 5.5. A clear image of the azimuthal orientation of the electrodes is visible in Fig. 3.3. To minimize direct axial drive feedthrough, the magnetron sideband (on the compensation electrodes) and axial drives (on the endcaps) corresponding to a detection scheme, are located on the opposite side of the plane z=0. Direct feedthrough of the direct cyclotron drive is minimized by use of a balanced drive, where the drive ν_c' is applied across two opposing quadrants of the ring and the detection is across the other quadrant [97].

Also shown in Fig. 5.5 are the high voltage electrodes capable of holding -3 kV for the confinement of high energy antiprotons (top HV endcap and degrader). Additional cylindrical electrodes, labeled Top HV #1 through #4, are used to

increase the antiproton capture efficiency by extending the trap length. A field emitting point (FEP) is included which serves as an electron source, and an HP 5082-2750 diode is directed into the trap for excitation of the electron cyclotron motion at 164 GHz.

5.3 Detection Sensitivity

The voltage signal V_F after the cryogenic pre-amplifier is

$$V_F^2 = (G_F IR)^2 + v_{noise}^2, \tag{5.9}$$

where IR is the signal from the center of mass oscillation and v_{noise} is the noise contributed from the resonant circuit and FET amplifier. The noise can be expressed as

$$v_{noise}^2 \approx (G_F v_R)^2 + v_{FET}^2. \tag{5.10}$$

The thermal Johnson noise v_R depends on the temperature of the effective resistor, and v_{FET} depends upon the FET temperature, tap ratio, 1/f noise that is frequency dependent. The 1/f noise can be large for the axial antiproton amplifier at 1.9 MHz and we have observed that it varies from one batch of FET's to another.

The cryogenic FET pre-amplifier increases the power to drive a 50 Ω transmission line. The voltage gain G_F is of the order one. The voltage output V_1 from the first external amplifier is then

$$V_1^2 = (G_1 V_F)^2 + (v_{NF})_1^2, \tag{5.11}$$

where G_1 is the voltage gain of the amplifier and v_{NF} is the amplifier noise. The relative noise contributions from the rest of the external amplifiers are less by a factor of G. The observed voltage after further amplification G is approximately

$$V_{rms} \approx GV_1 = GG_1\sqrt{(IR)^2 + (v_{noise})^2 + (\frac{v_{NF}}{G_1})^2}. \tag{5.12}$$

For optimum signal to noise we need to maximize the ratio,

$$\frac{V_{Signal}}{V_{Noise}} = \frac{IR}{\sqrt{(v_{noise})^2 + (v_{NF}/G_1)^2}}. \tag{5.13}$$

Table 5.2: Detection sensitivity

Calibration of v_{noise} for each Tuned Amplifier

Amplifier	V_{rms} $(G_1G = 10^3)$ $(G_1 = 3.2, (v_{NF})_1 = 0.4nV/\sqrt{Hz})$	$V_{rms}/\sqrt{Hz}$	v_{noise}(IR=0) $(V_{rms}/GG_1 - v_{NF}/G_1)$
$\nu_z(\overline{p})$	230μV (BW=1kHz)	$7.3\mu V/\sqrt{Hz}$	3.1 $nV/\sqrt{Hz}$
$\nu_z(e^-)$	30μV (BW=1kHz)	$0.95\mu V/\sqrt{Hz}$	0.8 $nV/\sqrt{Hz}$
$\nu_c'(\overline{p})$	10μV (BW=1kHz)	$0.32\mu V/\sqrt{Hz}$	0.2 $nV/\sqrt{Hz}$

Actual Amplification Used for Measurements

Amplifier	type	v_{NF}	G_1	G	V_{rms}(typical)	$V_{rms}/\sqrt{Hz}$
$\nu_z(\overline{p})$	Anzac	0.4 $nV/\sqrt{Hz}$	3.2	316	73μV (BW=100 Hz)	7.3 $\mu V/\sqrt{Hz}$
$\nu_z(e^-)$	Anzac	0.4 $nV/\sqrt{Hz}$	3.2	316	80μV (BW=100 Hz)	9.0 $\mu V/\sqrt{Hz}$
$\nu_c'(\overline{p})$	Janel	1.5 $nV/\sqrt{Hz}$	11.4	375	14μV (BW=100 Hz)	1.4 $\mu V/\sqrt{Hz}$

Required Image Current to Yield Unity Signal to Noise

Amplifier	v_{noise}	v_{NF}/G_1	$\sqrt{(v_{noise})^2 + (v_{NF}/G_1)^2}$	I/$\sqrt{Hz}$)
$\nu_z(\overline{p})$	3.1 $nV/\sqrt{Hz}$	0.13 $nV/\sqrt{Hz}$	3.1 $nV/\sqrt{Hz}$	4.4×10^{-15}
$\nu_z(e^-)$	0.3 $nV/\sqrt{Hz}$	0.13 $nV/\sqrt{Hz}$	0.3 $nV/\sqrt{Hz}$	1.8×10^{-15}
$\nu_c'(\overline{p})$	0.1 $nV/\sqrt{Hz}$	0.5 $nV/\sqrt{Hz}$	0.5 $nV/\sqrt{Hz}$	6.4×10^{-15}

For a fixed detection scheme (fixed R, tap ratio, trap size, noise sources) the only way to improve the signal to noise is to increase I. Thus we either increase the particle number (though this may require a broader bandwidth) or the particle amplitude (by driving harder) to increase the signal to noise. Unfortunately, larger amplitudes may result in the particle sampling imperfections in the trapping fields. For sufficiently high energies the measured frequencies may include relativistic shifts.

In Table 5.2 the sensitivity of each amplification chain is tabulated along with the necessary particle oscillation so that the induced signal is large enough to be observed above the noise. Coherent phase sensitive detection is a way to reduce the signal to noise requirements (and thus to reduce the required particle amplitudes and/or number). Since many of the measurements reported here are done by simply heating the motions, the parameters in Table 5.2 are useful for understanding the limitations of the technique.

5.4 Trap Voltage

The quality and stability of the dc voltage applied to the trap is important especially with regard to the stability of the axial frequency. Standard cells are often used to bias traps for high precision measurements because, when thermally regulated, they offer a potential source with very little noise.

For the measurements reported in this thesis, we have used a commercially available Fluke 5440 Voltage Calibrator. It is IEEE compatible allowing us to externally control the voltage, and has a two polarity range from -1100 V to +1100 V dc. The device is intended for use as a calibrator accurate to $\pm 4 \times 10^{-6}$ when calibrated against national standards and remains within specifications in a temperature range of $\pm 5°C$. The Fluke is useful since we want to compare opposite polarity particles. The output of opposite polarities has been measured at $\pm$ 71.6 Volts to be in agreement to better than 0.0005 Volts using a Fluke 8840A multimeter.

The noise specifications in our typical operating range of $\pm$ 22-275 Volts is 35

μV (BW 0.1 Hz to 10 Hz), and 150 μV (BW 10 Hz to 10 kHz). Voltage fluctuations of 150μV may shift (or broaden) the axial frequency by 10^{-6} corresponding to an uncertainty of 2×10^{-8} in the cyclotron frequency of a trapped antiproton. The source is improved by filtering and these specifications are not limiting for most of the observations reported.

The output of the Fluke V_0 is applied directly to the ring electrode of the trap and the endcaps are grounded. This is the superposition of $-V_0/2$ with the boundary conditions defined in Fig. 3.1 . With V_0 applied to the ring and the endcaps grounded, the compensation potential V_{comp} to applied is

$$V_{comp} \equiv V_c + \frac{V_0}{2} \tag{5.14}$$

The optimum tuning potentials are calculated to be $V_c = 0.381V_0$ or $V_{comp} = 0.881V_0$.

The compensation potential is obtained from the same supply using a voltage divider. From Eq. 3.6, less stability is required in V_c than in V_0 by a factor of $D_2/C_2 \approx 8 \times 10^{-3}$. The divider is adjustable with a 10 turn trimpot over a range $V_{comp} = 0.856V_0$ to $V_{comp} = 0.943V_0$.